Batteries & Supercaps

Research Article
doi.org/10.1002/batt.202500406

Chemistry Europe
European Chemical Societies Publishing

www.batteries-supercaps.org

Enhancing the Energy Density of Zn-Ion Capacitors Using Redox-Active Choline Anthraquinone Electrolyte

Sumana Brahma, Jonathan Huddleston, Emine Kapancik Ulker, and Abhishek Lahiri*

Owing to ease of recyclability, high theoretical capacity (820 mAh g^{-1}), safety, facile manufacture, and high energy density, Zinc-ion capacitors (ZICs) are emerging as promising capacitors and have attracted substantial attention. However, aqueous ZICs frequently encounter several difficulties, comprising low coulombic efficiency, low Zn anode deposition/stripping efficiency, hydrogen evolution, fast capacity decay, and Zn dendrite formation. Hence, to inhibit the formation of Zn dendrites, it is important to tune the electrolyte and the electrode/electrolyte interface. Herein, the key problems are tackled by using choline-based electrolytes. ZIC with $ZnCl_2$ in the presence of choline chloride yields good capacity and inhibits Zn dendrite formation due to the adsorption of choline at the interface. To further increase the energy density of the device, redox-active choline anthraquinone sulphonate (ChAQS) additives are synthesized and incorporated into the $ChCl/ZnCl_2$ system. The constructed graphene-based aqueous ZIC with the novel (ChCl/ ChAQS /$ZnCl_2$) electrolyte system shows a high specific capacity of 460 F g^{-1} and a high energy density of 185 Wh kg^{-1} at 0.25 A g^{-1}. These outcomes demonstrate an innovative pathway to fabricate biobased redox electrolytes for emerging sustainable energy storage devices.

1. Introduction

Even though high energy-density lithium-ion capacitors are commercially used in the rechargeable battery market, the growing concerns related to the high cost, limited lithium resources, low power density, and the volatility of organic electrolytes restrict their further progression.[1–3] To overcome such issues, low-cost, advanced energy storage systems, such as metal-ion capacitors, integrated with both the advantages of batteries and capacitors, have turned out to be a new, emergent topic. Among all the monovalent (Li^+, Na^+, and K^+) and multivalent (Mg^{2+}, Ca^{2+}, and Al^{3+}) metal-ion, zinc-ion capacitors (ZICs) have secured more attention due to their high theoretical capacity (819 mAh g^{-1}), nontoxicity, low oxidation–reduction potential (−0.76 V vs SHE) safety, and relatively low cost.[4–8] The charge storage kinetics of the capacitor cathode assure high power density associated with the adsorption/desorption of ions, whereas the zinc anode provides the high energy density related to the Zn deposition/stripping process.[9,10] Carbon-based cathode materials, such as graphene, own the advantages of high conductivity, outstanding structural stability, and outstanding mechanical strength.[11,12]

Moreover, aqueous ZICs are regarded as the most promising class of capacitors for energy storage due to their environmental benignity, facile manufacture, high operational safety, and almost 2 orders higher magnitude of ionic conductivities (≈1 S cm^{-1}) than the volatile organic electrolytes (≈1–10 mS cm^{-1}).[13–15] Generally, aqueous ZICs contain various zinc salts, such as zinc sulphate, zinc chloride, zinc tetrafluoborate, zinc bis (trifluoromethanesulfonylimide), etc..[16–18] Among them, few studies have been published for ZIC with $ZnCl_2$ salt electrolytes. Wiu et al. reported ZIC with a nonaqueous deep eutectic solvent electrolyte comprising $ZnCl_2$ and ethylene glycol, which showed a capacity of 78.6 mA h g^{-1}.[19] Wang et.al. had reported ZIC with hydrogel electrolytes containing $ZnCl_2$ salt that exhibits a high energy density of 217 Wh kg^{-1} at a power density of 450 W kg^{-1}.[20] However, aqueous ZICs often encounter numerous difficulties, such as narrow electrochemical windows, fast capacity decline, hydrogen evolution reaction (HER), poor coulombic efficiency, Zn dendrite formation, and low metallic Zn anode deposition/stripping efficiency.[21–23] Modifying the hydrogen-bonding network within the electrolyte and uplifting the overpotential for HER at the zinc anode can significantly mitigate HER activity.[24,25] Therefore, it is vital to develop electrolytes that can inhibit Zn dendrite formation and has a wide electrochemical window.[26] Ionic liquids (ILs) are potential electrolytes that can be introduced with zinc salt-containing aqueous electrolytes to resolve these issues. ILs have high thermal stability, low vapor pressure, high electrical conductivity, and a wide electrochemical window.[27,28] Moreover, another outstanding characteristic of ILs is that the van der Waals and coulombic interactions between cations and anions can be reformed by modifying ILs.[29]

S. Brahma, J. Huddleston, E. Kapancik Ulker, A. Lahiri
Department of Chemical Engineering
Brunel University London
Uxbridge UB8 3PH, United Kingdom
E-mail: abhishek.lahiri@brunel.ac.uk

E. Kapancik Ulker
Department of Chemistry
Faculty of Science and Arts
Recep Tayyip Erdogan University
Rize 53100, Turkey

Supporting information for this article is available on the WWW under https://doi.org/10.1002/batt.202500406

Further, to enhance the specific capacitance and the specific energy density of the capacitors, the electrolyte systems can be modified by incorporating redox-active additives.[7,30,31] Redox-active electrolytes, including electrochemically active species, undertake reversible redox reactions, thereby improving the charge storage process.[32–34] Further, during Zn plating, the electrolyte additives tend to adsorb onto the zinc dendrites due to the localized electric field enhancement, thereby preventing Zn ion deposition at the protrusions.[35] Moreover, the dendrite growth can also be suppressed by modulation of the solvation structure. Some electrolyte additives can modify the solvation structure of Zn ions by decreasing the number of coordinated H_2O molecules, which can suppress the parasitic side reactions and enhance the desolvation process.[36] A few reports have proved that incorporating organic redox additives in aqueous electrolytes increased the energy density of ZIB and ZIC.[37,38] Usually, quinone derivatives are the most prevalent redox-active electrolytes used in ZIB and ZICs. The anthraquinone (AQ) molecules are encouraging additives due to their high solubility, outstanding stability, and exclusive solvation behavior.[39,40] Further, Aziz et al. showed that the solubility of AQ can increase further with the introduction of the $-SO_3$ group, which could improve the solubility of AQ and electrochemical redox reversibility.[41,42] However, anthraquinone derivatives display higher solubility and redox reversibility in acid/basic electrolytes, resulting in poor device performance due to corrosion. Therefore, a pH-neutral electrolyte such as ILs with an AQ derivative might be a better choice for high-performance storage devices. Song et al. employed real-time X-ray imaging, revealing that IL additives can suppress the dendrite growth, which makes it a promising electrolyte for ZICs.[43]

In the present work, we have synthesized choline anthraquinone sulphonate (ChAQS) as a redox additive and studied its applicability as a novel biobased aqueous electrolyte for ZIC. By optimizing the electrolyte composition using choline chloride (ChCl), $ZnCl_2$, and ChAQs, the fabricated ZICs exhibit high specific capacity (≈460 F g^{-1} at 0.25 A g^{-1}) and a high energy density of 185 Wh kg^{-1}.

2. Experimental Section

2.1. Materials

Choline chloride (ChCl) 98%, zinc chloride ($ZnCl_2$) 99.5%, sodium anthraquinone sulphonate (AQSNa) 98%, cation exchange resin (Amberlite IRC 120(H) ion exchange resin), anion exchange resin (Amberlite IRA 900(Cl) ion exchange resin), N-methyl pyrrolidine (NMP), polyvinylidene fluoride (PVDF), and super-p were used as received from Sigma-Aldrich. Graphene (surface area 800 m^2) was procured from Nanografi Nano Technology, Germany.

2.2. Synthesis of ChAQS

The column was flushed with 1 M H_2SO_4 to precondition the strong cation exchange resin and further washed with distilled (DI) water until the pH of the column outlet solution was 7. Afterward, 100 mL aqueous solution AQSNa (8 mM) was flushed into the pretreated columns three times to confirm that the AQSNa fully transformed into anthraquinone suphonate (AQSH). Similarly, to precondition the strong basic anion exchange resin, 1 M NaOH was flushed through the column until no precipitation was observed in the solution at the outlet after adding the silver nitrate solution. Further, 24 mL of ChCl (100 mM) was added into the respective column three times to alter it into the base analog, choline hydroxide (ChOH).

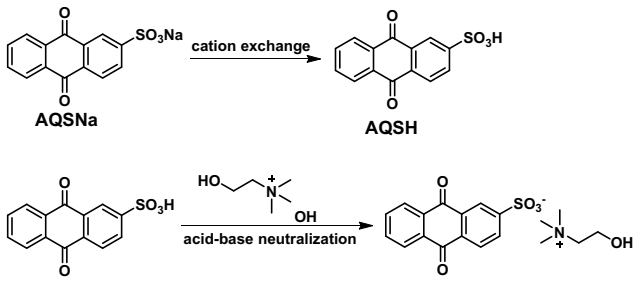

Scheme 1. Synthesis of ChAQS

The equimolar ratio of both ChOH and AQSH was mixed in a round-bottom flask to prepare ChAQS. The solvent water in the reaction mixture was removed under reduced pressure distillation. The wet solid was dried at 70 °C under a vacuum for 48 h. The prepared yellow solid of ChAQS was characterized by ^1H spectroscopy. The comparison of ChAQS and AQSNa is shown in Figures S1 and S2, Supporting Information, where a stark difference in the aliphatic region is observed due to a change in the cation. **Scheme 1** shows the synthesis of ChAQS.

2.3. Apparatus and Procedure

Bruker Avance 500 MHz was used to record the ^1H nuclear magnetic resonance (NMR) using an external solvent of D_2O. The XRD was analyzed using Bruker D8 Advance XRD, Germany, using a monochromatic Cu kα radiation at a wavelength of $\lambda = 1.5406$ and a LynxEye™ silicon strip detector. The IR spectra were analyzed in Shimadzu IR-Spirit.

For developing the carbon electrodes, a homogeneous slurry was obtained by mixing graphene (90%), PVDF (5 wt%), and super-P carbon (5 wt%) in NMP solvent. The slurry was coated onto a graphite foil by doctor blading with a mass loading of 2 mg cm^{-2}. All the electrochemical measurements, including the cyclic voltammetry (CV) and galvanostatic charge–discharge (GCD), were conducted employing the Biologic model VSP-3 E potentiostat controlled by EC-Lab software. Graphene | electrolytes-soaked glass fiber | Zn was used with (1.8 M ChCl/1 M $ZnCl_2$/3 mM ChAQS) electrolytes for ZIC devices.

From the obtained data, the specific capacitance of the cell was calculated based on Equation (1).[44]

$$C_{spec,cell} = \frac{I\Delta t}{m_{tot}\,\Delta V} \quad (1)$$

where m_{tot} (g) is the total mass of the active material (Graphene), I (A) is the applied current, ΔV (V) is the potential range, and Δt (s) is the discharging time.

Research Article
doi.org/10.1002/batt.202500406
Chemistry Europe
European Chemical Societies Publishing

The energy density (E_{Cell}) (Wh kg^{-1}) and power density (P_{Cell}) (W kg^{-1}) of the cell were determined using Equation (2) and (3).[45]

$$E_{cell} = \frac{C_{spec,cell}}{7.2} \quad (2)$$

$$P_{cell} = \frac{E_{cell}}{\Delta t} \quad (3)$$

3. Results and Discussions

3.1. Physical Characterization

The infrared spectroscopy (IR) of ChAQS (**Figure 1**) shows a broader vibrational stretching frequency of OH at 3500–3200 cm^{-1} in ChAQS than AQSNa, which is related to the hydroxyl group of choline and the intermolecular hydrogen bonds. The substitution of sodium ions by choline ions formed extremely hydrophilic phases in ChAQS compared to AQSNa.

However, the peaks at 1290 cm^{-1}, 1670 cm^{-1}, and 1590 cm^{-1} correspond to the vibrational stretching frequency of phenyl group, C=C and C=O groups for both AQSNa and ChAQS, which confirms the unaltered quinone structure after anion exchange.[39] The additional peaks of choline mostly overlapped with the anthraquinone sulphonate (AQS). However, based on the ^{1}H NMR in Figures S1 and S2, Supporting Information, along with FTIR studies, it is evident that we could successfully synthesize ChAQS.

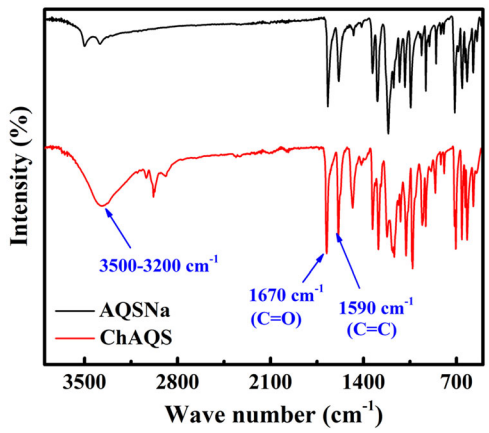

Figure 1. IR spectrum of ChAQS and AQSNa.

3.2. Electrochemical Characterization

The ZIC was first fabricated with a graphene cathode, Zn anode, and 1 M $ZnCl_2$ electrolyte. The electrochemical performance of the fabricated ZIC was initially examined using CV (**Figure 2**a). The CV curves were carried out at different scan rates (5 to 200 mV s^{-1}) between the voltage range of 0.3 V and 2.0 V. The symmetric curves were obtained at a lower scan rate, but there is a distortion of the symmetric curve at a higher scan rate. The capacitive behavior of ZIC was assessed by the GCD technique at various current densities of 0.5-10 A g^{-1}, Figure 2b. A symmetric GCD profile was obtained at high current densities, indicating capacitive behavior of the electrode. Moreover, Figure 2c shows the calculated specific capacitances of ZIC at different current densities. The maximum specific capacitance was 190 F g^{-1} at 0.5 A g^{-1}.

However, the ZIC shows poor rate capabilities at high current densities in 1 M $ZnCl_2$ electrolyte, which could be attributed to electrochemically induced hydrolysis of Zn^{2+} ions leading to the formation of $Zn(OH)_2$/ZnO.[46] This issue can further compromise the reversibility of the Zn metal anode, resulting in poor stability.

To resolve these issues, the electrolyte was modified with ChCl. It has been shown that the quaternary ammonium cation can adsorb on the Zn anode surface to suppress the development of dendrite growth.[47] **Figure 3** shows the GCD curve of the ZIC device with 1 M $ZnCl_2$ and different concentrations of ChCl (0.4 M to 2 M) at 0.5 A g^{-1} current density. At low concentrations of ChCl, the capacity diminished compared to $ZnCl_2$ electrolytes. However, with the increase in the concentration of ChCl, the capacity enhances (Figure 3). The obtained specific capacity is 154, 168, 180, 190, 204, and 176 F g^{-1} at 0.5, 0.75, 1.0, 1.5, 1.8, and 2 M concentrations of ChCl, respectively. Therefore, the

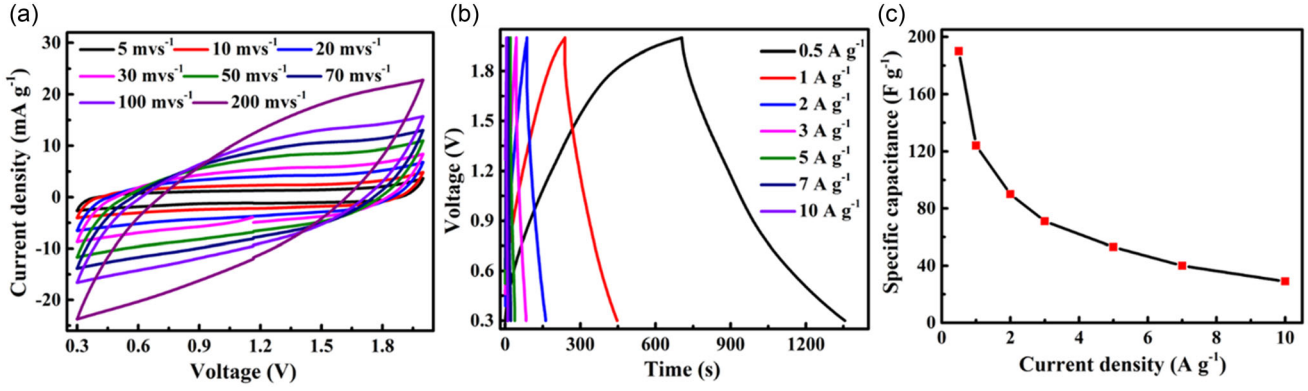

Figure 2. a) CV curve at different scan rates, b) GCD at different current densities, and c) $C_{s,2E}$ as a function of current densities of ZIC in 1 M $ZnCl_2$ electrolyte.

Research Article
doi.org/10.1002/batt.202500406
Chemistry Europe
European Chemical Societies Publishing

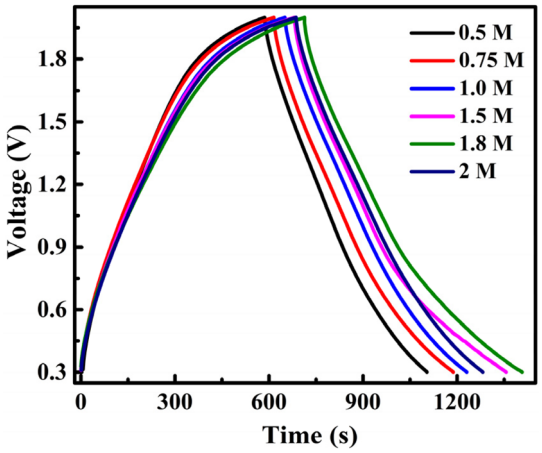

Figure 3. GCD curves at a current density of 0.5 A g^{-1} for the ZIC device in different molar concentrations of ChCl in 1 M $ZnCl_2$ electrolyte.

optimized concentration of ChCl of 1.8 M was used for further electrochemical studies.

To clarify the stability of the electrolyte systems (1.8 M ChCl/1 M $ZnCl_2$) for ZICs, a Zn deposition/stripping study was carried out in a Zn/Zn symmetric cell. The cycling stability of the electrolyte was analyzed by continuing the plating/stripping study at 2 mA cm^{-2} current for a period of more than 180 h (**Figure 4**a). The symmetric cell showed a low deposition/stripping overpotential of ≈30 mV throughout the cycling, confirming the long-term stability of the electrolyte. The SEM (Figure 4b) of Zn did not show any dendrite formation even after 180 h of cycling. The energy dispersive X-ray (EDX) (Figure S3) showed only the presence of Zn, Cl, and O. The Cl comes from some unwashed electrolyte, whereas the oxygen is due to surface oxidation of the sample during the transfer to the microscope.

To understand the influence of ChCl in the electrolyte, corrosion and hydrogen evolution behavior of Zn electrode in the $ZnCl_2$ and $ZnCl_2$+ChCl electrolytes were investigated using the Tafel plot (Figure 4c). The Tafel extrapolation was employed to determine the corrosion potential (E_{corr}) and current densities (I_{corr}). An increase in E_{corr} and a decrease in I_{corr} indicate the corrosion process slowed down due to enhanced corrosion resistance.[47,48] Accordingly, E_{corr} and I_{corr} were determined to be −0.98 V and 0.71 mA cm^{-2} in $ZnCl_2$, and −0.99 V and 0.22 mA cm^{-2} in $ZnCl_2$+ChCl, respectively. The shift toward a more negative E_{corr} and significantly lower I_{corr} in $ZnCl_2$+ChCl suggests that adding ChCl to $ZnCl_2$ improves the corrosion resistance of the solution. No changes in the corrosion were observed on the addition of ChQAS. Additionally, linear scan voltammetry (LSV) was performed to evaluate the hydrogen evolution performance of the Zn electrode in different electrolytes (Figure 4d). To reach 10 mA cm^{-2}, a potential of −1.06 V is required in $ZnCl_2$ and −1.1 V in $ZnCl_2$+ChCl. The more negative potential required in $ZnCl_2$+ChCl suggests a higher overpotential for HER, which is

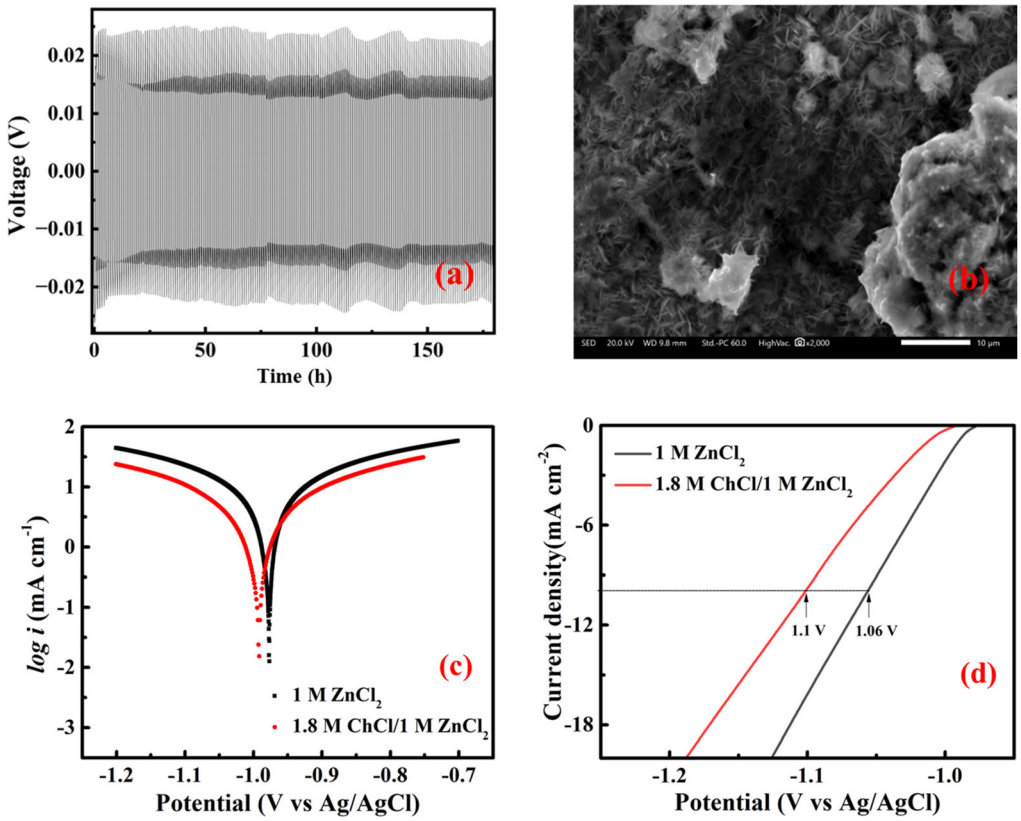

Figure 4. a) The Zn plating/stripping in a Zn/Zn symmetric cell with 1.8 M ChCl/1 M $ZnCl_2$ electrolyte at 2 mA cm^2 with a sweep duration of 10 min over 180 h, b) SEM image of Zn electrodes after cycling, c) corrosion curves of Zn electrode, and d) LSV curves of Zn electrode in $ZnCl_2$ and ChCl/$ZnCl_2$ electrolyte.

consistent with the corrosion studies. Furthermore, the electrochemical window of the electrolytes showed that addition of ChCl widens the electrochemical window (Figure S4).

The optimized electrolyte was then used to study the ZIC performance. The GCD curves of the 1st, 10th, and 50th cycles of the ZIC device with 1.8 M ChCl/1 M $ZnCl_2$ are compared (**Figure 5**) with the GCD curves of the ZIC device with 1 M $ZnCl_2$. It is observed that the capacity does not fade on using 1.8 M ChCl/1 M $ZnCl_2$ even after the 50th cycle, whereas a significant capacity loss was observed for 1 M $ZnCl_2$ electrolyte.

To understand the changes in the electrochemical behavior in the presence of ChCl, CVs were examined at different scan rates (5–100 mV s^{-1}) in the potential range of 0.3–2.0 V, as shown in **Figure 6**a. The CV curves show a capacitive behavior even at a 100 mV s^{-1} scan rate. Furthermore, GCD curves were recorded at different current densities (Figure 6b), and the maximum specific capacity of 205 F g^{-1} at 0.5 A g^{-1} and 102 F g^{-1} at 10 A g^{-1} was observed (Figure 6c). Hence, the capacity retention, even at high current density, is enhanced after adding ChCl into the $ZnCl_2$ electrolyte system.

To enhance the specific capacitance of ZIC, redox-active ChAQS was added. To optimize the concentration of the ChAQS, the CV was carried out with different concentrations of ChAQS (0-4 mM ChAQS/1.8 M ChCl/1 M $ZnCl_2$). **Figure 7**a shows a sharp oxidation peak at 0.65 V and a corresponding reduction peak at 0.5 V after adding the additive. The redox peaks correspond to the quinol/quinone redox reaction on the graphene electrode. With increasing concentration of ChAQS from 0.5 mM to 3.0 mM, the integrated area of the CV increases, leading to an increase in capacitance. However, with the concentration above 3 mM, the current associated with the redox reaction diminishes. This may be due to the effect of overcrowding of the ions, resulting in the inhibition of ion mobility toward the electrode/electrolyte interface.[49,50]

To further evaluate the concentration effect on capacitance, GCD was carried out at different concentrations of ChAQS (Figure 7b) at the current density of 0.5 Ag^{-1}. The GCD curves show the sharp redox process at 0.65 V 0.5 V, similar to the CV curves, due to the faradaic reaction. The corresponding capacitance values are calculated from GCD curves and presented in Figure 7c. The curve shows that the maximum capacitance is 390 F g^{-1} for 3 mM ChAQS. Therefore, further studies were performed with 3 mM ChAQS/1.8 M $ChCl_2$/1 M $ZnCl_2$ electrolyte.

To elucidate the electrolyte effect (3 mM ChAQS/1.8 M ChCl/1 M $ZnCl_2$) on the suitability for ZICs, Zn deposition/stripping behavior in a Zn/Zn symmetric cell was conducted. It is evident

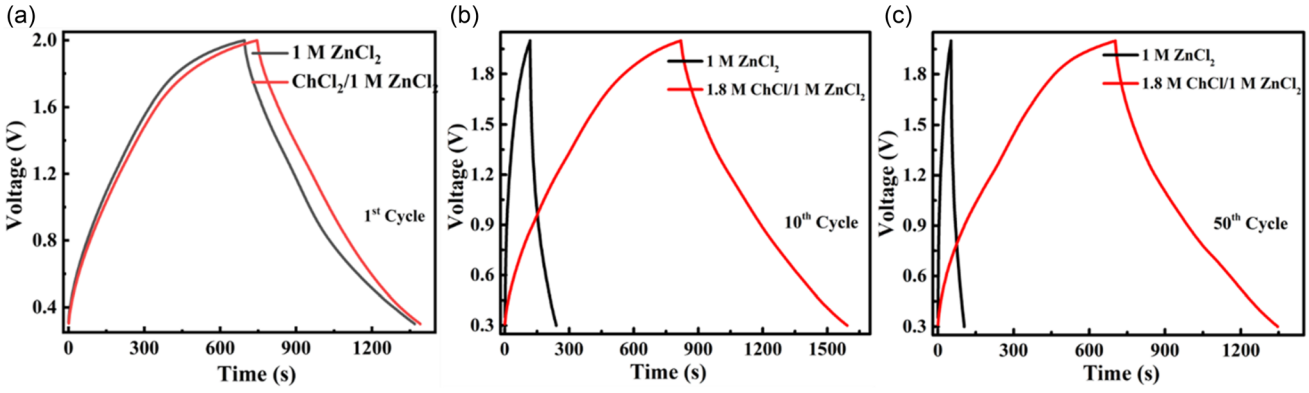

Figure 5. GCD curves at a current density of 0.5 A g^{-1} for ZIC device with 1.8 M ChCl/1 M $ZnCl_2$ and 1 M =$ZnCl_2$ a) 1st cycle, b) 10th cycle, and c) 50th cycle.

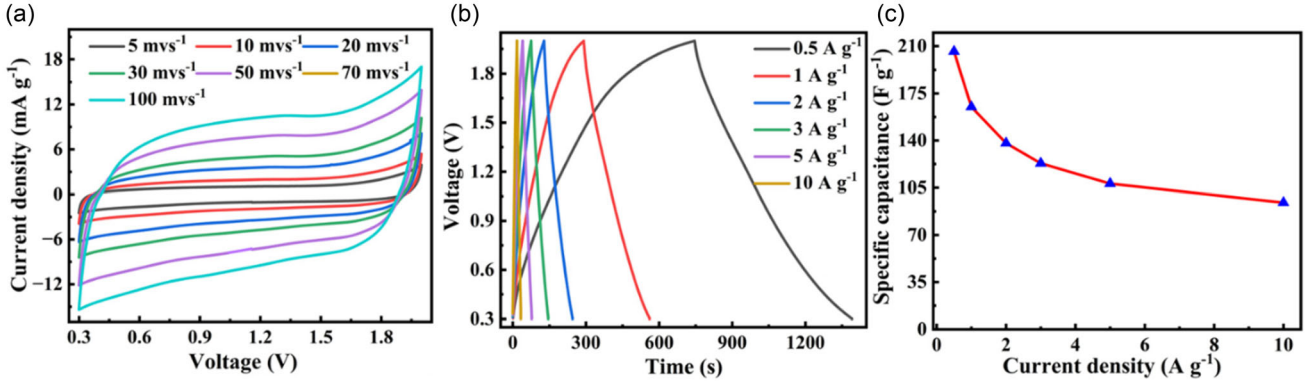

Figure 6. a) CV curve at different scan rates, b) GCD at different current densities, and c) $C_{s,2E}$ as a function of current densities of ZIC in 1.8 M ChCl/1 M $ZnCl_2$ electrolyte.

Research Article
doi.org/10.1002/batt.202500406
Chemistry Europe
European Chemical Societies Publishing

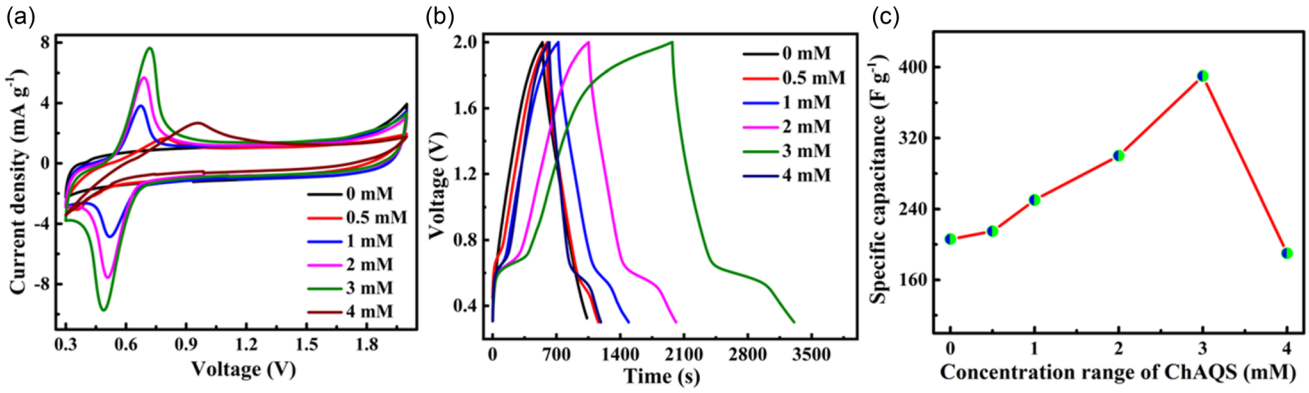

Figure 7. a) CV curve at different scan rates, b) GCD at different current densities, and c) $C_{s,2E}$ as a function of current densities of ZIC in x mM ChAQS/ 1.8 M ChCl/1 M $ZnCl_2$ electrolyte.

that on cycling in both the electrolyte systems at a current density of 2 mA cm^{-2} with a capacity of 0.5 mAh cm^{-2}, the stability of the Zn deposition/stripping process does not reduce even after 180 h (**Figure 8**a). From the SEM images (Figure 8b), it is evident that there is no zinc dendrite formation even after 180 h of cycling.

XRD of the Zn electrode after long-term galvanostatic testing in electrolytes of $ZnCl_2$, $ZnCl_2$+ChCl, and $ZnCl_2$+ChCl+ChAQS are compared in Figure 8c , which represents the characteristic peak of Zn (ICDD 78-9363). The ratio of the (101) to the (002) diffraction peaks shown in Table ST1 varies depending on the composition of the electrolyte. In pure $ZnCl_2$, the ratio was calculated to be 0.85712, suggesting moderate preferential growth along the (101) plane. After the addition of ChCl, the ratio decreased to 0.75417, indicating a shift in preferred orientation toward the (002) plane. However, the addition of both ChCl and ChAq increased the ratio to 0.97055, suggesting a reorientation favoring the (101) plane. These results indicate that the electrolyte composition significantly affects the nucleation and the growth process.[51,52]

To investigate the optimized redox electrolyte on ZIC, CVs were conducted at different scan rates (1–100 mV s^{-1}) as shown in **Figure 9**a. Both the current density and the peak separation increase with the scan rates due to a diffusion-controlled process. Moreover, with the increase in scan rate, there is a sharp decrease in current in the CV curve below 0.45 V, which may be attributed to some Zn deposition along with quinone/quinol redox reaction. Based on the CV, the possible reaction mechanism during charging would be that the Zn^{2+} ion is reduced to Zn metal, whereas the ChAQS electrolyte in aqueous medium is reduced at the cathode side and forms a quinol derivative. During discharge, the Zn metal anode is oxidized to Zn^{2+} and the quinol derivative is oxidized to quinone form. The overall reaction mechanism can be as follows

$$Zn + Q + 2H^+ \leftrightarrow Zn^{2+} + QH_2 \quad (4)$$

where Q is the quinone form and QH_2 is the quinol form.

GCD curves were recorded at different current densities of 0.25 to 10 A g^{-1}, as shown in Figure 9b. The distortion of symmetric triangular GCD curves confirms the dominant pseudocapacitance behavior of quinol/quinone redox reaction. The faradaic reaction is consistent even at high current density. The estimated value of the specific capacitance of the ZIC from the GCD curve was 460 F g^{-1} and 190 F g^{-1} at a current density of 0.25 A g^{-1} and 10 A g^{-1}, respectively (Figure 9c).

Figure 9c also displays the coulombic efficiency versus current density plot, and the coulombic efficiency is ≈86% at a current density of 0.25 A g^{-1}, which progressively escalates to 100% at around 10 A g^{-1} as the contribution of the faradaic component decreases with the current density. The Ragone plot

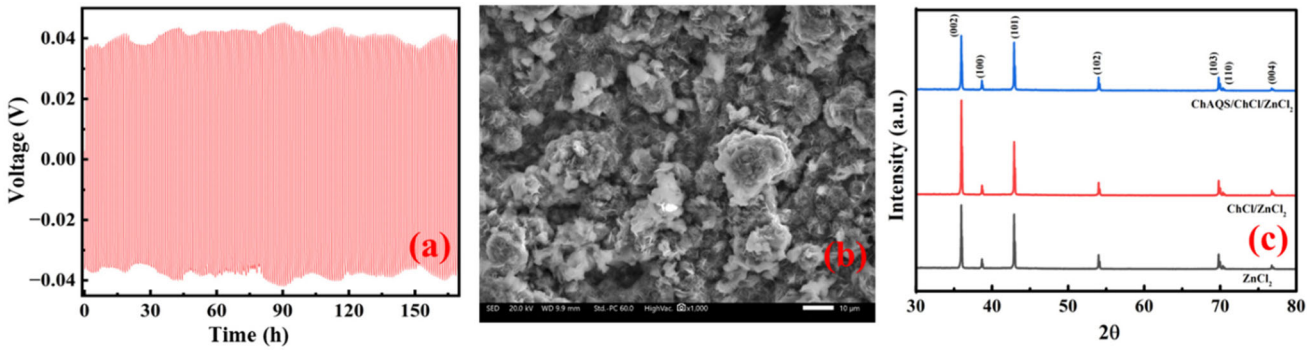

Figure 8. a) The Zn plating/stripping in a Zn/Zn symmetric cell with 3 mM ChAQS/1.8 M ChCl/1 M $ZnCl_2$ electrolyte at 2 mA cm^2 with a sweep duration of 10 min over 180 h, b) SEM images of the Zn electrodes after cycling, and c) XRD spectra of the Zn electrode after long-term galvanostatic testing in electrolytes of $ZnCl_2$, $ZnCl_2$/ChCl, and ChAQS/ ChCl/$ZnCl_2$.

Research Article
doi.org/10.1002/batt.202500406
Chemistry Europe
European Chemical Societies Publishing

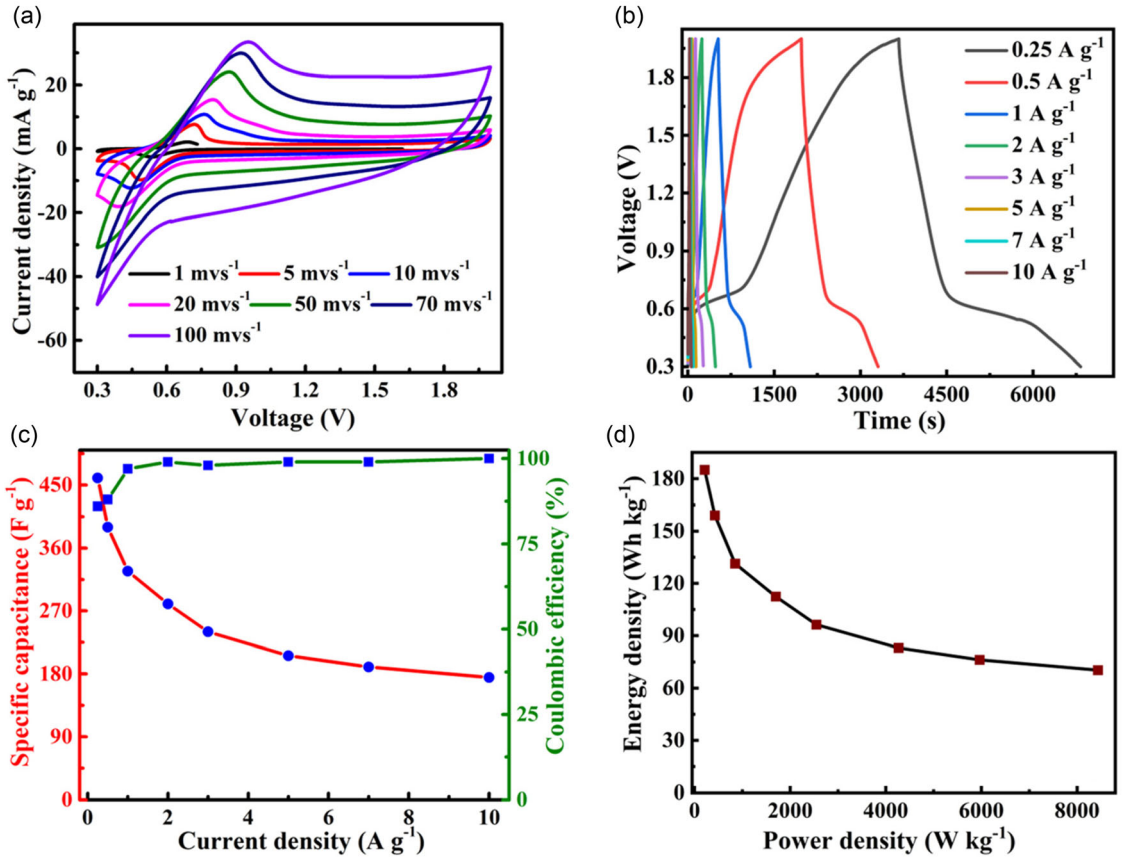

Figure 9. a) CV at various scan rates, b) GCD at various current densities, c) specific capacitance and coulombic efficiency as a function of different current densities, and d) Ragone plot of ZIC with 3 mM ChAQS/1.8 M ChCl/1 M $ZnCl_2$ electrolyte system.

(Figure 9d) shows an energy density of 185 Wh kg^{-1} and the power density of 0.5 kW kg^{-1} that can be achieved at a current density of 0.25 A g^{-1}. A comprehensive literature report on ZIC with redox-active additives performance is presented in Table ST2, which clearly shows that the energy density achieved here is at par, if not higher than others reported in the literature.

To understand the contribution from capacitive and faradaic processes, the relationship between the charge storage kinetics and the capacity of the electrode was investigated by Dunn's method. The capacitive contributions in the 3 mM ChAQs/1.8 M ChCl/1 M $ZnCl_2$ system were examined by Equation (4) and (5).[53]

$$i = a\upsilon^{b} \tag{5}$$

$$\log i(V) = b\log(\upsilon) + \log a \tag{6}$$

where i and ν denote the current and scan rate, respectively, and b is a constant. In general, $b = 1$ represents the ideal electrical

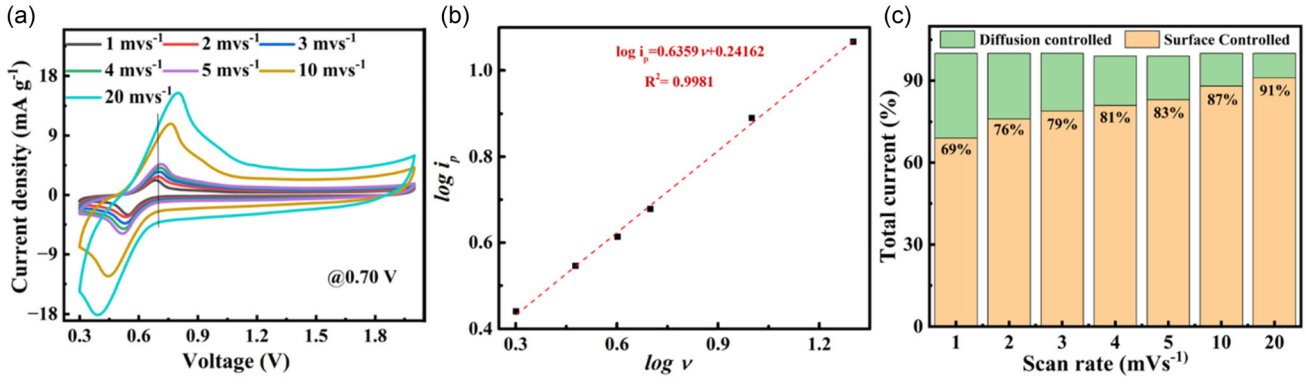

Figure 10. a) CV curves of the graphene/Zn electrode at various scan rates ranging from 1 to 20 mV s^{-1} in the electrolyte of 3 mM ChAQs/1.8 M ChCl/1 M $ZnCl_2$ electrolyte system, b) *log(i)* versus *log(v)* curves relationship for peak as shown in Figure 4a, and c) capacity contribution ratio at various scan rates from 1 to 20 mV s^{-1}.

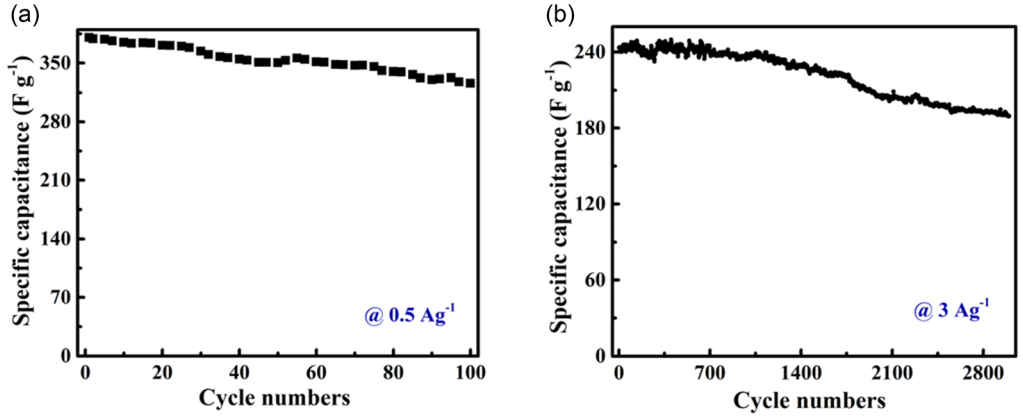

Figure 11. The stability curve for ZIC with 3 mM ChAQS/1.8 M ChCl/1 M $ZnCl_2$ at a current density of a) 0.5 A g^{-1}, and b) 3 A g^{-1}.

double layer capacitance (EDLC) process, whereas $b = 0.5$ signifies the faradaic process corresponding to diffusion kinetics due to redox reaction.

Figure 10a shows the CV curve at different current densities (1 to 20 mV s^{-1}) from which the contribution of capacitive and faradaic processes was determined. The logarithmic value of peak current (shown by the vertical line in Figure 10a) and the scan rate studies are demonstrated in Figure 10b, which shows a straight line and the b values calculated from the curve. The ZIC device with 3 mM ChAQs/1.8 M ChCl/1 M $ZnCl_2$ system showed a b values of 0.64, which indicates that both capacitive and faradaic processes are involved in the storage mechanism for the graphene electrode. The percentage of total current arising out of surface-controlled and diffusion-controlled processes is given in Figure 10c. As shown in Figure 10c, with the increase in scan rate from 1 to 20 mV s^{-1}, the corresponding capacitive contribution ratio increases accordingly.

Finally, the stability of ZIC with 3 mM ChAQS/1.8 M ChCl/1 M $ZnCl_2$ electrolyte was evaluated at a current density of 0.5 A g^{-1} (**Figure 11**a), where an initial capacity of 375 F g^{-1} was achieved and 90% of the initial capacity was retained after 100 cycles. The capacity decay that occurs might be due to the formation of byproducts at a low current density, which is a common phenomenon in aqueous ZIBs/ZICs.[54]

At a higher current density of 3 A g^{-1}, an initial capacity of 240 F g^{-1} was observed, and a stability of 82% capacitance retention was achieved even after 3000 GCD cycles (Figure 11b). The loss in capacity might be related to changes in the interfacial processes, which will need further investigation. However, the current study shows new avenues for exploiting biobased redox molecules for energy storage.

4. Conclusions

In summary, we have shown a promising ZIC using a $ZnCl_2$-based electrolyte containing choline anthraquinone redox species for the first time. It was observed that the electrolyte containing only $ZnCl_2$ had issues with stability and rate capability. The addition of choline chloride with optimized concentration significantly improves the stability of the ZIC. To enhance the energy density of the ZIC, ChAQS additives led to a redox process on graphene, which improved the specific capacitance to 460 F g^{-1} at 0.25 A g^{-1}. A relatively stable capacity was achieved with a capacity retention of 82% for 3000 cycles at 3 A g^{-1}.

Acknowledgements

The authors thank the EPSRC (EP/W015129/1) for funding this project. E.K.U. thanks the Science and Technology Council of Turkey (TUBITAK) for the support provided through the 2219 program (Project No: 1059B192301430).

Conflict of Interest

The authors declare no conflict of interest.

Data Availability Statement

Data have been made available in Brunel University London's repository via Brunel Figshare database.

Keywords: choline antraquinone sulphonate · ionic liquids · pseudocapacitance · redox-active electrolytes · zinc-ion capacitors

[1] Y. Chen, Y. Kang, Y. Zhao, L. Wang, J. Liu, Y. Li, Z. Liang, X. He, X. Li, N. Tavajohi, B. Li, *J. Energy Chem.* **2021**, *59*, 83.
[2] T. Kim, W. Song, D.-Y. Son, L. K. Ono, Y. Qi, *J. Mater. Chem. A* **2019**, *7*, 2942.
[3] A. Manthiram, *J. Phys. Chem. Lett.* **2011**, *2*, 176.
[4] H. Tang, J. Yao, Y. Zhu, *Adv. Energy Mater.* **2021**, *11*, 2003994.
[5] R. Bahadur, B. Wijerathne, A. Vinu, *ChemSusChem* **2024**, *17*, e202400999.
[6] J. Sun, B. Luo, H. Li, *Adv. Energy Sustain. Res.* **2022**, *3*, 2100191.
[7] S. Brahma, A. Panda, V. Kaliginedi, A. Chutia, A. Lahiri, *J. Power Sources*, **2025**, *641*, 236843.
[8] J. Li, Y. Gao, R. Holze, S. Li, E. Mijowska, X. Chen, *Batteries Supercaps* **2023**, *6*, 202300175.
[9] J. Yang, M. A. Bissett, R. A. W. Dryfe, *ChemSusChem* **2021**, *14*, 1700.
[10] Z. Huang, T. Wang, H. Song, X. Li, G. Liang, D. Wang, Q. Yang, Z. Chen, L. Ma, Z. Liu, B. Gao, J. Fan, C. Zhi, *Angew Chem.* **2021**, *133*, 1024.
[11] Z. Sun, S. Chu, X. Jiao, Z. Li, L. Jiang, *J. Energy Storage* **2024**, *75*, 109571.

[12] D. Sui, M. Wu, K. Shi, C. Li, J. Lang, Y. Yang, X. Zhang, X. Yan, Y. Chen, *Carbon* **2021**, *185*, 126.
[13] L. Dong, W. Yang, W. Yang, Y. Li, W. Wu, G. Wang, *J. Mater. Chem. A* **2019**, *7*, 13810.
[14] Y. Shao, F. Shen, Y. Shao, *ChemElectroChem* **2021**, *8*, 484.
[15] K. Wu, X. Liu, F. Ning, S. Subhan, Y. Xie, S. Lu, Y. Xia, J. Yi, *ChemSusChem* **2025**, *18*, e202401251.
[16] Q. Yang, Z. Huang, X. Li, Z. Liu. H. Li, G. Liang, D. Wang, Q. Huang, S. Zhang, S. Chen, C. Zhi, *ACS Nano* **2019**, *13*, 8275.
[17] L. Li, S. Jia, Z. Cheng, C. Zhang, *ChemSusChem* **2023**, *16*, e202300632.
[18] C. Wang, Z. Pei, Q. Meng, C. Zhang, X. Sui, Z. Yuan, S. Wang, Y. Chen, *Angew. Chem.* **2021**, *60*, 990.
[19] H. Tiana, R. Chenga, L. Zhanga, Q. Fanga, P. Mab, Y. Lva, F. Wei, *Mater. Lett.* **2021**, *301*, 130237.
[20] C. Wang, Z. Pei, Q. Meng, C. Zhang, X. Sui, Z. Yuan, S. Wang, Y. Chen, *Angew. Chem.* **2021**, *60*, 990.
[21] A. Khosrozadeh, M. Chang, P. Vahdatkhah, J. Liuand, O. Voznyy, *J. Mater. Chem. A* **2022**, *10*, 20431.
[22] L. Zhang, Z. Liu, G. Wang, J. Feng, Q. Ma, *Nanoscale*, **2021**, *13*, 17068.
[23] Z. Liu, G. Li, T. Cui, A. Borodin, C. Kuhl, F. Endres, *J. Solid State Electrochem.* **2018**, *22*, 91.
[24] Y. Bai, D. Deng, J. Wang, Y. Wang, Y. Chen, H. Zheng, M. Liu, X. Zheng, J. Jiang, H. Zheng, M. Yi, W. Li, G. Fang, D. Wang, Y. Le, *Adv. Mater.* **2024**, *36*, 2411404.
[25] S. Zhan, Y. Guo, K. Wu, F. Ning, X. Liu, Y. Liu, Q. Li, J. Zhang, S. Lu, J. Yi, *Chem. Eur. J.* **2024**, *30*, e202303211.
[26] R. Yan, M. Antonietti, M. Oschatz, *Adv. Energy Mater.* **2018**, *8*, 1800026.
[27] K. Dong, S. Zhang, J. Wang, *Chem. Commun.* **2016**, *52*, 6744.
[28] X. Gan, C. Zhang, X. Ye, L. Qie, K. Shi, *Energy Storage Mater.* **2024**, *65*, 103175.
[29] J. Zeng, J. Yang, C. Yi, J. Huang, L. Zheng, X. Wang, *J. Power Sources* **2024**, *620*, 235222.
[30] L. Wei, Y. Chen, Z. Huang, S. Zheng, X. Guo, *Energy Storage Mater.* **2023**, *58*, 30.
[31] Y. Li, M. Zhang, H. Lu, X. Cai, Z. Jiao, S. Li, W. Song, *Adv. Funct. Mater.* **2024**, *34*, 2400663.
[32] Z. Wu, Z. Huang, R. Zhang, Y. Hou, C. Zhi, *Int. J. Extrem. Manuf.* **2024**, *6*, 062002.
[33] C. Liu, X. Xie, B. Lu, J. Zhou, S. Liang, *ACS Energy Lett.* **2021**, *6*, 1015.
[34] W. Qin, N. Zhou, C. Wu, M. Xie, H. Sun, Y. Guo, L. Pan, *ACS Omega* **2020**, *5*, 3801.
[35] B. Luo, H. Wang, C. Chen, L. Liu, K. Wu, H. Li, D. Ye, Y. Li, L. Cui, J. Qiao, *J. Colloid Interface Sci.* **2024**, *675*, 639.
[36] S. Zhan, Y. Zhu, Y. Li, X. Liu, F. Ning, Y. Xie, S. Lu, Y. Xia, J. Yi, *Adv. Funct. Mater.* **2025**, 2507573.
[37] Y.-Y. Hsieh, H.-Y. Tuan, *Energy Storage Mater.* **2024**, *68*, 103361.
[38] Z. Tie, Z. Niu, *Angew. Chem.* **2020**, *59*, 21293.
[39] Y. Yang, D. Wang, J. Zheng, X. Qin, D. Fang, Y. Wu, M. Jing, *Electrochim. Acta* **2023**, *452*, 142292.
[40] J. D. Hofmann, S. Schmalisch, S. Schwan, L. Hong, H. A. Wegner, D. Mollenhauer, J. Janek, D. Schröder, *Chem. Mater.* **2020**, *32*, 3427.
[41] M. R. Gerhardt, L. Tong, R. G. Bombarelli, Q. Chen, M. P. Marshak, C. J. Galvin, A. A. Guzik, R. G. Gordon, M. J. Aziz, *Adv. Energy Mater.* **2017**, *7*, 1601488.
[42] Q. Chen, Y. Lv, Z. Yuan, X. Li, G. Yu, Z. Yang, T. Xu, *Adv. Funct. Mater.* **2022**, *32*, 2108777.
[43] Y. Song, J. Hu, J. Tang, W. Gu, L. He, X. Ji, *ACS Appl. Mater. Interfaces* **2016**, *8*, 32031.
[44] S. Brahma, K. Ramanujam, R. L. Gardas, *Ind. Eng. Chem. Res.* **2022**, *61*, 12073.
[45] Y. Jing, F. Ning. Z. Jing, L. Rui, L. Feng, D. Yuchuan, Y. Zhenglong, *ACS Omega* **2019**, *4*, 15904.
[46] Z. Yea, Z. Caoa, M. O. L. Chee, P. Dong, P. M. Ajayanc, J. Shena, M. Ye, *Energy Storage Mater.* **2020**, *32*, 290.
[47] Z. Gong, Z. Li, P. Wang, K. Jiang, Z. Bai, K. Zhu, J. Yan, K. Ye, G. Wang, D. Cao, G. Chen, *Energy Mater. Adv.* **2023**, *4*, 0035.
[48] P. Liu, X. Ling, C. Zhong, Y. Deng, X. Han, W. Hu, *Front. Chem.* **2019**, *7*, 656
[49] C. Cruz, E. Lomba, A. Ciach, *J. Mol. Liq.* **2022**, *346*, 117078.
[50] J. Huang, M. Li, M. J. Eslamibidgoli, M. Eikerling, A. Groß, *JACS Au* **2021**, *1*, 1752.
[51] S. Wu, Z. Hu, L. Ren, J. Huang, J. Luo, *eScience*, **2023**, *3*, 100120
[52] K. Mohammadzadeh, U. K. Kumer, A. Lahiri, *J. Electrochem. Soc.* **2025**, *172*, 052505
[53] K. M. Albalawi, M. Al-Dossari, A. M. Saeedi, R. H. Althomali, G. F. B. Solre, M. Sadiq, S. U. Asif, *J. Energy Storage* **2024**, *104*, 114576.
[54] S. Brahma, J. Huddleston, A. Lahiri, *ChemElectroChem* **2024**, *11*, e202400511.

Manuscript received: May 27, 2025
Revised manuscript received: June 27, 2025
Version of record online: July 16, 2025